ARTICLE

Received 00th January 20xx, Accepted 00th January 20xx

DOI: 10.1039/x0xx00000x

Robust Three-dimensional Nanotube-in-Micropillar Array Electrodes to Facilitate Size Independent Electroporation in Blood Cell Therapy

Xuan Liu, a, f An-Yi Chang, a, f Yifan Ma, b Liping Hua, a Zhaogang Yang, f b and Shengnian Wang a

Blood is an attractive carrier for plasmid and RNA based medicine in cell therapy. Electroporation serves as its favorable delivery tool for simple operation, quick internalization, minimum cell culture involvement, and low contamination risk. However, the delivery outcomes of electroporation heavily depend on the treated cells such as their type, size, and orientation to the electric field, not ideal for highly heterogeneous blood samples. Herein a new electroporation system was developed towards effective transfection to cells in blood regardless their large diversity. By coupling replica molding and infiltration coating processes, we successfully configured a three-dimensional electrode comprised of a polymer micropillar array on which carbon nanotubes (CNTs) are partially embedded. During electroporation, cells sag between micropillars and deform to form conformal contact with their top and side surface. The implanted CNTs not only provide a robust conductive coating for the polymer micropattern, but also have their protruded ends face the cell membrane vertically everywhere with maximum transmembrane potential. Regardless their largely varied sizes and random dispersion, both individual blood cell type and whole blood samples were effectively transfected with plasmid DNA (85% after 24 hrs and 95% after 72 hrs, or 2.5-3.0 folds enhancement). High-dose RNA probes were also introduced which regulate better the expression levels of exogenous and endogenous genes in blood cells. Besides its promising performance on non-viral delivery route to cell-related studies and therapy, the invovled new fabrication method also provides a convenient and effective way to construct flexible electronics with stable micro/nanofeatures on the surface.

Introduction

Blood is an attractive source in cell therapy because of its superior biocompatibility and quick accessibility of a variety of functional cells in large quantity. 1-3 Classical blood cell immunotherapy utilizes certain type of purified white blood cells (WBCs) such as dendritic cells, and stimulates them into therapeutic cells in three costly and labor-intensive procedures: (i) harvesting patient cells via leukapheresis; (ii) in vitro culturing the isolated monocytes into dendritic cells (DCs); (iii) loading DNA/RNA probes in matured DCs and injecting them back to patient.4 Unlike these classic cell vaccination that involves painful collection, week-long in vitro modification and expansion, and re-injection of patient immune cells via second surgery, pioneer research work has successfully demonstrated that antigen-encoding mRNA probes could be directly loaded in cells of whole blood after immediate isolation from patient body to serve as RNA

vaccines to subsequently activate T-cells and induce antitumor immune responses. 5.6 Besides encapsulating target mRNA in various types of WBCs, this emerging whole blood immunotherapy strategy expects erythrocytes, the most prominent cellular population in blood, to serve as the perfect protecting carriers for most target RNA probes to avoid quick degradation from nuclease because of their enriched RNase-inhibitor environment. 7.8 Compared to classic blood cell immunotherapy, this new whole blood therapy route is less invasive, not amenable for repeated administration, and of minimal cost (i.e., time, specialized resources, and often proprietary formulations). 6

For both types of blood cell therapy, effective delivery of genetic probes to blood cells is essential, in which viral vectors are commonly used. Although having high transfection efficiency in host cells and sustained expression of target genes, viral transduction is associated with significant risk to permanent genome modification of host cells and inflammation during clinic trials. 9,10 Non-viral delivery strategies with known lifetime are therefore preferred in future clinical practice for safety consideration. But the adoption of non-viral delivery methods may occur only if they can accomplish sufficient transfection efficiency and cell viability comparable to their viral counterparts. Among various non-viral delivery strategies, electroporation is favored in these applications for its balance of operation simplicity, quick

^a Center for Biomedical Engineering and Rehabilitations, Institute for Micromanufacturing, Louisiana Tech University, PO Box 10137, Ruston, LA, 71222 USA

b. Department of Radiation Oncology, The University of Texas Southwestern Medical Center, Dallas, TX 75390, USA

[‡]These authors contribute equally

^{*}Corresponding author, Zhaogang Yang, Zhaogang.Yang@UTSouthwestern.edu; Shengnian Wang, $\underline{swang@latech.edu}.$

probe delivery, and flexibility on cell and therapeutic probe types. ¹¹ These features allow only minimum time and cost on cell preparation, perfect compliance to the operation room delivery requirement for the mRNA vaccination practice using whole blood. As a matter of fact, a commercial electroporation system has been used in the aforementioned pioneer research work, demonstrating the feasibility of electroporation in whole blood cell therapy. ⁶

Although commercial electroporation systems serve as a promising exogenous DNA or RNA delivery tool in general, its current configuration carries several drawbacks that impede its application in blood cell therapy, namely its indiscriminate, high-voltage pulse treatment on blood cells of various sizes. The samples of whole blood therapy include various red blood cells (RBCs) and WBCs, obviously a mixture of cells with different types, sizes, and morphologies (e.g., RBCs: 6-8 µm; leukocytes: 12-15 μm; dendritic cells: 6-15 μm; monocytes: 15-30 µm).13 Even for classical blood immunotherapy that uses a designated type of WBCs, cells from the same batch could still show a size variation of 10 μm or more. According to the electroporation theory, transient and reversible breakdown of the cell membrane can be achieved only when the transmembrane potential (TMP, ΔV_m) surpasses the threshold of the cell membrane capacitance, which is given as:

$$\Delta V_{m} = fgE_{ext}rcos\theta \tag{1},$$

in which f is the geometrical factor of a cell (equal to 1 for a perfect sphere), g adds corrections for dielectric property difference of a cell and its surrounding medium, $E_{\rm ext}$ is the electric field strength (in V/cm), r is the radius of a cell (in cm), θ is the angle between $\textit{E}_{\rm ext}$ and the cell membrane surface. $^{\rm 12}$ Therefore, effective electroporation is not only related to the pulse field strength, but also the electrical properties and status of the treated cells such as their size and morphology. According to Equation 1, TMP on cells is strongly correlated with the size of the treated cells. In another word, large cells experience higher imposed TMP than small cells. When cells of various size populations are placed in the electric field of a commercial cuvette setup, only those within appropriate size range receive reversible breakdown of their cell membrane for successful payload delivery. Other cells, either fail to generate large enough permeable area to allow effective probe uptake due to the insufficient TMP (for smaller cells) or receive severe damage on their plasma membrane to prevent quick recovery and eventual survival because of their overdosed TMP (for larger cells) during electroporation, even under recommended protocols which are likely optimized on the dominant size populations. Besides cell size, the orientation of the cell membrane surface to the electric field is also important, with the maximum poration occurs at 0° and 180° angle locations, as shown in Figure 1a. Unfortunately, these issues did not attract enough attention in the past due to the lack of simple but effective tools to specify the pulse treatment on individual cells. Such needs become more critical in blood cell therapy considering their various cell types and large size diversity, which is particularly urgent in the transfection of whole blood cell samples.

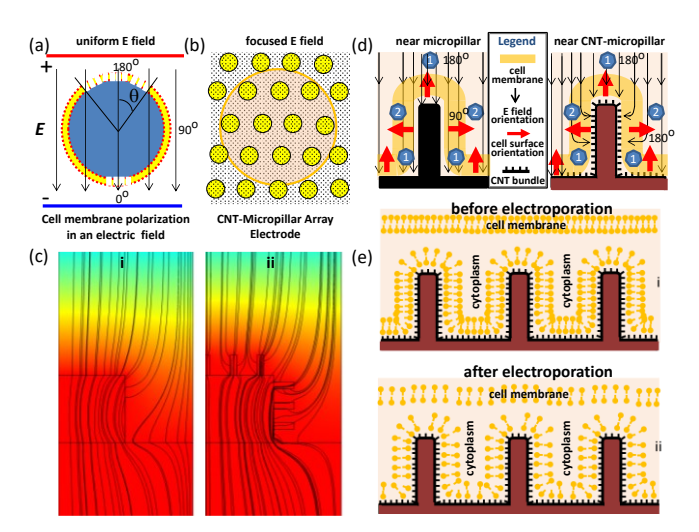


Figure 1. The working principle of the carbon nanotube implanted micropillar array electroporation (CNT-BME). (a) Schematic of the cell membrane polarization in an electric field (poration area on a cell occurs near 0° and 180° orientation with the electric field); (b) cell size-independent treatment mechanism on a CNT-implanted micropillar array electrode (poration area is distributed based on the number and size of micro/nanoelectrodes); (c) COMSOL simulation on the electric field focusing effect around electrodes (I: electrode with micropillar array alone; II: electrode with 3D CNT bundles imbedded on top and side surface of micropillars); (d) orientations of the electric field and the cell membrane surface on top and side of micropillar electrodes without CNTs (near 180° on top and 90° on side surface of micropillars) and with CNT implantation (near 180° on both top and side surface of micropillars) when cell sagged in the micropatterned electrodes; (e) the status of lipid bilayer structure membrane of a cell that settles on micropillar array before (i) and after (ii) electroporation.

To overcome these limitations and meet the needs for both types of blood therapy practice, we recently developed a three-dimensional (3D) electrode configuration with carbon nanotube implanted in micropillar array and used it to accomplish cell size independent electroporation to blood cells (designated as "CNT-BME"). In CNT-BME, cells are sandwiched between two parallel plate electrodes with well-patterned micropillar array texture on whose surface carbon nanotubes (CNTs) are partially implanted in bundles. When cells lay on these electrodes, the number of micropillars each cell faces varies with their membrane surface area or the size of cells. But the pore formation is independent of the random dispersion status of cells as micropillars form a regular array pattern on the electrode surface (Figure 1b). Like in other electroporation setups with micro-/nanoscale features, 14-32 micropillars on CNT-BME electrodes help focus the electric field when pulses are imposed on the cell membrane (Figure 1c i), which locally porate those area with a micrometer resolution (Figure 1b). With CNTs partially implanted in the polymer micropattern, their free-standing end protrudes out of the surface of micropillars to further leverage the pulse

focusing (Figure 1c_ii) and specify the electroporation area with nanometer accuracy (Figure 1b). Because of gravity and imposed pressure when the loaded solution is squeezed between the two electrodes, cells settling on micropillar arrays sag in the gap space between micropillars (Figures 1d & 1e_i), leaving the cell membrane on the CNT-micropillar top in stretched states which are found beneficial for electroporation than round-shaped, suspended cells.33-35 As CNTs are implanted on both the top and side surface of micropillars, such a 3D nanotube-in-micropillar configuration allows those nanoelectrodes to vertically face the sagged cell membrane surface nearly everywhere under conformal contact. Unlike the micropillar electrode without CNTs in which the deformed cell membrane along its side surface holds a 90° orientation with the imposed electric field ("E field") as shown in Figure 1d_i, the new nanotube-in-micropillar electrodes maintain a close to 0° or 180° facing angle between the orientation of the cell membrane surface and the "E field" on both their top and side surface (Figure 1d_ii). According to Equation 1, the transmembrane potential is therefore maximized nearly everywhere over the deformed cell, creating a desired electroporation configuration. As the consequence, a looser lipid bilayer structure is expected to form across the entire cell membrane during electroporation (Figure 1e_ii) to allow higher permeability than other electroporation systems. Given all these advantages, this 3D nanotube-in-micropillar electroporation is expected to improve the transfection of plasmid and oligonucleotides in heterogeneous blood cells despite their various sizes, positions, and orientations.

Besides aforementioned advantages this CNT-BME system also brings a new fabrication method that makes robust conductive coating on electrodes to tolerate needed high current and/or voltage spikes in cell electroporation. It not only gets rid of traditional metal electrodes (e.g., aluminum) used in commercial systems which release unwanted metal ions (e.g., Al3+) into cells, ^{26, 36, 37} but also avoid quick detachment of the conductive layer from electrodes coated by thin film methods (e.g., electrophoretic deposition, physical vapor deposition, or solution casting) that are widely adopted in many micro/nanoscale electroporation systems. 26-32 Unlike these electrodes that the thin metal coating has only weak binding forces with the micro/nanoscale structure, we here identify a facile way to produce micropatterned electrodes with robust conductive coating through partially implanting CNTs in polymer microstructures. Such an electrode configuration is engineered by coupling a micromolding process using soft lithography with surface implantation of CNTs in polymer through resin infiltration, as illustrated in Figure 2 (detailed in section 2.3). The uncovered part of CNTs in the produced composite electrodes serves as numerous nanoscale electrodes while the rest portion entangled in the polymer matrix to form an essential conductive base. When used in electroporation, such partial implantation configuration offers robust CNT coating and excellent electrical conductivity in long-term or repeated use. Lymphoblasts cell lines alone (e.g., K562 cells), whole blood samples, and their mixtures with different populations were used to examine

electroporation performance on this CNTs-implanted micropillar array electrode. The transgene expression of GFP plasmids as well as down regulation of several target genes using siRNA and miRNA oligonucleotides were evaluated quantitatively.

Experimental

Materials and Reagents

SU-8 2002 photoresist was purchased from Microchem Inc. Single-wall carbon nanotubes (SWCNT) were purchased from carbon solution, Inc. PDMS resin (Sylgard 184 with a precursor to curing agent weight ratio of 10:1) was purchased from Dow Corning, Inc. Primer 4-inch, <100> silicon (Si) wafers with a resistivity of 5-10 Ω -cm and thickness of 500-550 μ m were purchased from WRS materials.

DNA plasmids probe with pMaxGFP reporter genes were purchased from Lonza, Inc. Small Interfering RNA (siRNA) used silencing pMaxGFP for (sense strand: CGCAUGACCAACAAGAUGAUU-3'; antisense strand: UCAUCUUGUUGGUCAUGCGGC-3') and miRIDIAN microRNA human has-miR-29b-3p mimic (miR29b, with a sequence: 5-UAGCACCAUUUGAAAUCAGUGUU-3) were synthesized by Thermo Scientific (Pittsburgh, PA). EZ Cap™ Cy5 EGFP mRNA (5-moUTP) was purchased from APExBIO Technology LLC. All cell culture reagents were purchased from Life Technologies (Carlsbad, CA) and all chemicals were purchased from Sigma-Aldrich unless specified.

Cell Culture.

K562 cells (ATCC, CCL-243) were used in electroporation test. These cells were cultured in RPMI 1640 medium (supplemented with 10% FBS, 1% L-Glutamine and Penicillin/streptomycin). All cultures were maintained at 37° C with 5% CO₂ and 100% relative humidity. Blood cells were separated from whole blood samples after centrifugation at 1,200 rpm for 5 min. The collected cell samples were further washed using OPTI-MEM I (a serum-free medium) three times. After mixing with K562 cells at different mixing ratios, the cell mixtures were used immediately in electroporation treatment.

Fabrication of CNT Implanted Micropillar Array Electrode

CNT implanted micropillar array electrodes were fabricated by coupling a micromolding process using soft lithography with surface implantation of CNTs in polymer through resin infiltration (Figure 2). A micropillar array pattern was first fabricated on a Si wafer using SU-8 2002 photoresist by a standard photolithography process. A pre-cleaned Si wafer was spun coated a 2- μ m thick SU-8 layer following a recommended protocol. ³⁸ The micropillar array pattern (2 μ m in diameter with a gap size of 2 μ m) was then transferred to the SU-8 layer on the Si wafer and served as the master template. To generate a conductive surface of micropillars, a rigid Si substrate that has a 500-nm thick oxide layer on the top as the insulation layer (Figure 2a_i) is taken as the electrode substrate, which is then coated with a fresh SU-8

layer (Figure 2b i). Separately, a PDMS (Syglard 184 from Dow Corning) daughter mold with negative replica of micropillar array pattern was made by soft lithography (Figure 2a_ii). SWCNTs were printed into microwell patterns on the PDMS mold through gentle rubbing between two PDMS blocks (Figure 2b_ii). Extra CNTs were then removed through repeating peeling using clean Scotch tape. The PDMS mold with thin CNT coating was then pressed into the SU-8 layer pre-coated on the Si substrate (Figure 2c). The PDMS mold and the Si substrate with SU-8 photoresist were then sandwiched between two glass slides using file clips and the whole set was then exposed under a UV light (UVP Blak-Ray™ B-100AP) through the PDMS mold side for 5 min, followed by baking in an oven at 100°C for 1 hour (Figure 2d). After cross-linking photoresist, the PDMS mold was removed, leaving CNT implanted polymer micropillar array on the Si substrate (Figure 2e). The protruded part of CNTs outside of the polymer microstructure serves as nanoelectrodes in electroporation while the rest entangled CNT network embedded inside the polymer matrix to form a continuous conductive base.

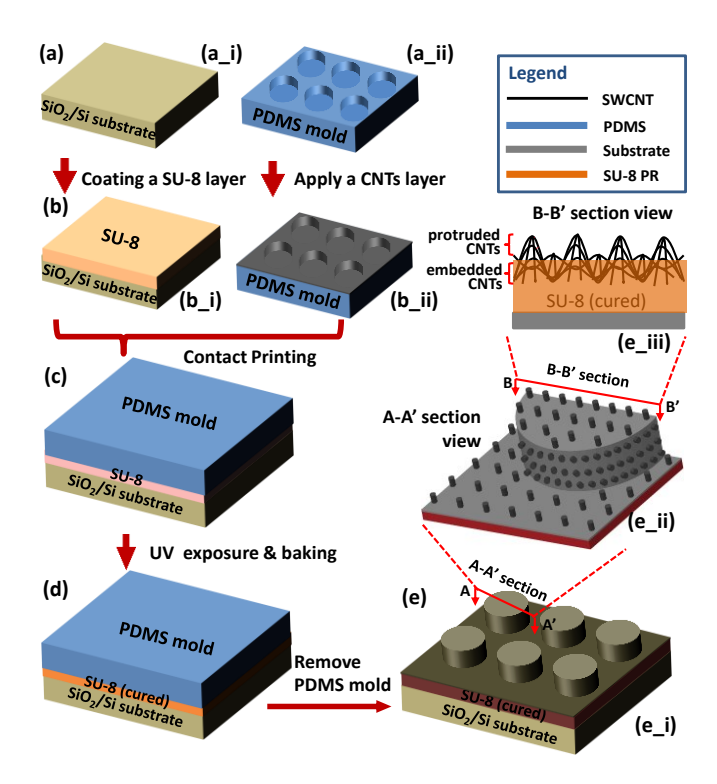


Figure 2. Schematic of the fabrication flowchart for three-dimensional nanoelectrodes with CNTs implanted in a polymer micropillar array pattern. Section drawings of an individual micropillar near section A-A' and a cross section view of section B-B' are shown in panels e_ii and e_iii, respectively.

CNT-BME Electroporation Setup and Operation Procedure

Cells were first centrifuged and re-suspended in fresh OPTI-MEM I at a density of 2.5×10^7 cells/ml. Plasmid DNA (pMaxGFP) of 1 μ g was then added. These samples (20 μ L

each) were loaded on the surface of CNT-BME electrode (connected to the positive electrode of a pulse generator). A piece of ITO-coated glass with a PDMS gasket (~200 μm thickness) was then placed from top, serving as the negative electrode. The cell solution was sandwiched between two electrodes and further squeezed until reaching the pre-set gap distance. A single, rectangular electrical pulse with pulse strength of 2.5 kV/cm and duration of 10 ms was then applied. The process, including cell loading, electroporation, and treated cell collection, takes less than 30 seconds among which most time is spent on sample loading and collection. After electroporation, cells were collected and further cultured in 12-well plates and at 37° C with 5% CO2 prior to analysis.

GFP Plasmid Transfection Efficiency and Cell Viability

The expression of pMaxGFP plasmids was examined qualitatively for cells with green fluorescence within representative area under an inverted fluorescence microscope (Olympus, Japan) and measured quantitatively by counting cells in a flow-cytometer (CytoFLEX PN B49006AE). For each sample, 10,000 events were counted, and the results were analyzed with Cytexpert software. The transfection efficiency of pMaxGFP is defined as the number of cells emitting fluorescence signal to the total number of cells in a sample (gated fluorescence signal of GFP). The GFP expression level is calculated as the mean fluorescence intensity of the whole counted cell population, which is correlated to the average dosage of plasmids delivered in individual cells. Their combination reflects a comprehensive picture of plasmid delivery and expression level in treated cells. Control samples were prepared under the same conditions except no electroporation treatment. They were used to exclude debris and gate forward (FSC) and side (SSC) light scatter signal ranges to define the counting cell population.

The cell viability was evaluated by an MTS cell proliferation assay (Promega, Madison, WI). Briefly, 100 μ L cell samples 24 hr post electroporation were transferred to a 96-well plate. CellTiter 96 AQueous One solution (Promega, Madison, WI) of 20 μ L was added to each well and all samples were incubated at 37°C for 1 hr. Absorbance was measured at 492 nm on an automated plate reader (Elx 800, Biotek, VT). The cell viability is calculated as the averaged absorbance signal ratio of an electroporated cell sample to the negative control sample (note: cells and plasmid mixtures experienced the same operation procedure except not applying electric pulses), after extracting the absorbance background from culture medium.

The Delivery and Down Regulation Efficiency of microRNA

The miR29b delivery efficiency was evaluated on the expression levels of both miR29b and its target genes in cells including CDK6, DNMT3B and MCL1. Total RNA was first reverse transcription into cDNA and a real-time PCR was then conducted. The expression level was determined by calculating the $\Delta\Delta$ Ct value and normalized to that of an endogenous control gene.

Total RNA Extraction

Total RNA was extracted using TRIzol reagent (Life Technologies, Carlsbad, CA). Cells were harvested by centrifugation and removal of culture medium. TRIzol reagent (250 µL) was then added to each sample (containing approximately 8-10×10⁵ cells) to lyse cells by pipetting several times. After incubating for 5 min at room temperature, the nucleoprotein complex was dissociated completely. Chloroform of 125 μL was then added to each sample tube, which was shaken vigorously for 15 seconds, followed by 3 min incubation at room temperature. Then all samples were centrifuged at 12,000 rpm for 15 min at 4°C. The upper aqueous phase was transferred into new tubes by gently pipetting. Isopropanol of 500 μL was then added in each sample. Followed further incubation for 10 min at room temperature, all samples were centrifuged again at 12,000rpm for 10 min at 4°C. After discarding the supernatant, 200 μL 75% ethanol was added into each tube to wash the RNA pellet. Samples were then vortexed briefly and centrifuged at 7,500 rpm for 5 min at 4°C. After removing the supernatant, the RNA pellets were dried in air for 5-10 min. RNase-free water (20µL) was then added into each tube and further incubated at 60°C for 10 min prior to PCR assay.

Reverse Transcription PCR

The Taqman® reverse transcription kit (Life Technologies, Carlsbad, CA) was used for microRNA reverse transcription. The reagents were first thawed on ice. A total volume of 15 μL reaction was prepared in a polypropylene tube, including 0.15 μL dNTP mix (100 mM), 1.0 μL MultiscribeTM RT enzyme (50 U/ μL), 1.5 μL 10 X RT PCR buffer, 0.19 μL RNase inhibitor (20 U/ μL), 4.16 μL nuclease free water, 3 μL primer and 5 μL RNA sample (1000 ng). The thermal cycler was programmed as follows: 30 min at 16 °C, 30 min at 42 °C, 5 min at 85 °C, and hold at 4 °C.

qRT-PCR Amplification

The resulting cDNA from reverse transcription reaction was amplified by qRT-PCR with TaqMan Gene Expression Master Mix (Thermo Scientific, Pittsburgh, PA). A total volume of 20 μL reaction was prepared in a polypropylene tube, including 10 μL TaqMan Gene Expression Master Mix, 1.0 μL 20 X Taqman assay, and 9 μL cDNA template. The thermal cycler was programmed as follows: 10 min at 95°C for polymerase activation, then 40 PCR cycles with 15 seconds at 95°C for denature and 1 min at 60°C for anneal. The relative gene expression was determined by the $\Delta\Delta$ Ct method. The mature miR-29b expression was normalized to endogenous control RNU48 and relative to the untreated control cells. The expression levels of CDK6, DNMT3B, and MCL1 mRNAs were normalized to endogenous controlled GAPDH and relative to the untreated controlled cells.

Whole Blood Sample Analysis

Different types of blood cells in whole blood samples were identified in microscopy images based on their morphology and/or size differences and quantified in flow cytometry as follows: subgroups of RBCs (erythrocytes + reticulocytes) and leukocytes were assigned according to their FSC intensity

difference while thiazole orange (TO) was used to label reticulocytes to further distinguish them from erythrocytes among RBCs. TO (0.5µg/ml) was incubated with cell samples for 20 mins and washed 3 times with PBS.

The loading efficiency of Cy5 labeled GFP mRNA in erythrocytes/reticulocyte/leukocytes population is quantified by the percentage of PE-positive events in flow cytometry. Live/dead assay measurement was done for instant cell viability evaluation following the vendor's protocol. Live cells are quantified by the percentage of FITC-positive ones (signal from fluorescent calcein after converting non-fluorescent calcein-AM by intracellular esterases) with the intensity threshold set by the negative control samples.

SEM Sample Preparation

A drop of cell solution was first applied on the micropillar electrode surface. Cells were then fixed with 2% glutaraldehyde in PBS buffer, followed by dehydration in a series of ethanol solutions with increasing concentration between 25 and 100% (25%/step, 20 min immersion in each step). The sample in 100% ethanol was further dried with CO₂ in a critical point drier to preserve the cell morphology. All scanning electron microscope (SEM) micrographs were acquired using a Hitachi 4800 SEM (operating voltage 3.0-5.0 kV). Before imaging, samples were sputter-coated with a 5 nm gold layer to improve electron conductance.

Electrochemical Impedance Spectroscopy (EIS) Analysis

EIS analysis was performed on an Autolab potentiostat (PGSTAT 302N, Metrohm USA) with NOVA 1.10.3 software. A test solution comprised of 5 mM K₄Fe(CN)₆/5mM K₃Fe(CN)₆ in 1M KCl was used. A two-electrode configuration was used with an alligator clip attached at the corner of the CNT-implanted micropillar array electrode as the working electrode. A Pt wire (1.5 mm in diameter from Alfa Aesar) was suspended in the testing solution as the reference/counter electrode. A sinusoidal AC signal with amplitude of 10 mV and frequencies ranging from 0.1 Hz to 100 kHz was applied. Nyquist plots were then made between the real impedance (Z') and imaginary impedance (-Z"). An equivalent circuit model including a solution resistor (Rs), two charge transfer resistances (Rp1, Rp2), two non-ideal capacitors (CPEs), and a Warburg element (W) was used to fit the Nyquist plot data for each case using NOVA 1.10.3 software.

COMSOL Simulation.

COMSOL (Mathworks, MA), was used to calculate the electric field in micropillar array electrodes with and without CNT coating using a finite-element method (FEM). We considered a symmetric geometry with half micropillar (1 $\mu m \times 1 \mu m$) and multiple CNT bundles (30 nm \times 200 nm) in the computation domain (6 $\mu m \times 2 \mu m$), as shown in supp Figure 1. An electric field (E= 2.5 kV/cm) was assigned across the top and bottom of the computation domain whose right-side boundary was set as insulated wall. The electrical conductivity of buffer, polymer micropillar, and CNTs was set as 0.8, 5×10^{-7} , and 5×10^6 S/m,

respectively. The electric potential distribution near the micropillar and CNT bundles was calculated.

Statistical Analysis.

All data points were represented as the mean ± standard deviation (SD) of triplicates, unless otherwise indicated. The significance analysis was performed with two-tailed t-test on triple duplicates unless specified.

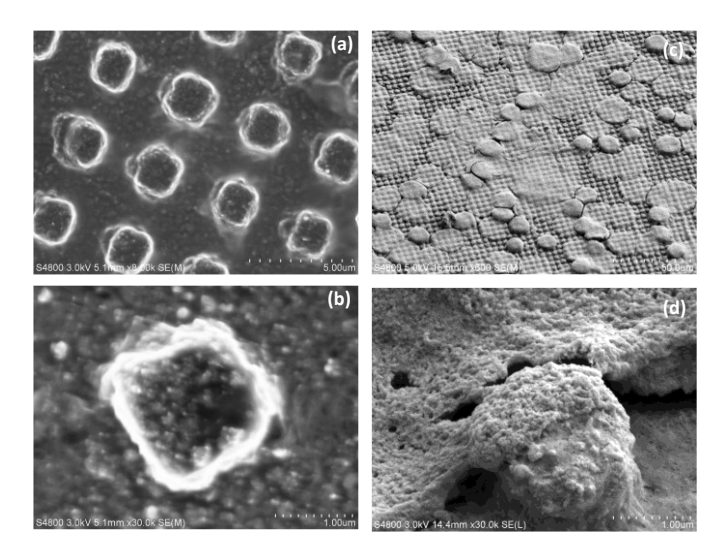


Figure 3. SEM images of CNT implanted micropillar array electrodes (a, b) and cells settling states on the top of CNT micropillar array electrode (c, d).

Results and discussion

Texture of CNT-implanted Micropillar Array Electrodes

Gold- or carbon-based conductive materials are often coated on electrode surface in many micro/nanoscale electroporation systems to provide the needed electrical conductivity. However, such a passively coated conductive layer easily falls off after high-voltage pulse strikes, making the long-term use or re-use of those electrodes or the entire device difficult. To solve this problem, we partially implanted CNTs onto the micropattern surface by allowing polymer resin to infiltrate into the voids among CNT bundle network during the micromolding stage. The embedded part of CNTs creates a conductive network inside and near the surface of the polymer micropattern to facilitate electron transfer for the entire electrode, while the uncovered part of CNTs protruded out of the micropillar surface, serving as individual nanoelectrodes to accomplish size independent electroporation with nanometer resolution. As shown in Figure 3a, a micropillar array pattern (2 µm in diameter with a gap size of 2 µm) is successfully produced by micromolding using a PDMS mold that has CNTs pre-cover its surface. CNTs can be clearly seen on the surface of both the polymer base (Figure 3a) and micropillars (Figure 3b), adding great roughness on the polymer surface. With CNTs partially implanted in polymer matrix, this creates numerous nanoelectrodes on both the side and top surface of micropillars in a three-dimensional format. When a cell lays on this CNT implanted micropillar array pattern,

part of the cell is supported by micropillars while the rest sags inside the gap in between due to gravity to form conformal contact with the side surface of micropillars (Figures 3c & 3d). This leaves the cell membrane sitting on the micropillar surface in a stretched state with thinner and more loosely packed lipid bilayer structure. As CNT nanoelectrodes protrude out of the surface of micropillars in three dimensions, the electric field aligns with the cell membrane (i.e., 0° or 180°) both on the top and side surface of micropillars (Figure 1d). According to Equation 1, maximum transmembrane potential is imposed nearly everywhere over the deformed cell membrane to create more polarized lipid bilayer structure during an electroporation treatment. These benefits are expected to leverage the cell membrane poration in larger area with more tiny pores, and as the consequence, improve the electroporation performance, namely better transfection efficiency and cell viability, on such nanotube-in-micropillar electrodes.

CNT-BME Enhancement on Plasmid Transfection

Figure 4a shows the typical phase contrast and fluorescent images of K562 cells 24 hours after being treated with plasmids reporting green fluorescence protein (GFP) by CNT-BME and cuvette-based traditional electroporation system ("denoted as "BE" in later discussions). Successful transfection is observed in both cases, but much more cells expressed GFP in CNT-BME treated samples than that in its BE counterpart. Their quantitative difference on GFPpositive cells was further measured with a flow cytometer, together with two other cases: one uses plain-plate electrode coated with CNTs (denoted as "CNT" in later discussions, as shown in supp Figure 2) and the other has polymer micropillar array electrode coated with gold (denoted as "BME" as in reference²⁵). Compared to a transfection efficiency of 31.5% ± 0.6% in the BE treatment, the GFP plasmid transfection was improved to 43.2% ± 3.1% for electroporation treated with CNT-coated plain plate electrodes (Figure 4b). The addition of ~12% was achieved due to the numerous nanoscale poration sites on the CNT-coated electrode. When the cell size independent electroporation was introduced (the "BME" case), this contributes significant delivery enhancement with the transfection efficiency reaching 70.3% ± 2.5%. Combining CNT implanted on arrays of micropillars (i.e., the "CNT-BME" treatment), the three-dimensional nanoelectrodes further leverages the transfection of GFP plasmids to 84.8% ± 1.0%. These results demonstrate the enhancement of plasmid transfection by CNT-BME in blood cells and the improvement is indeed attributed by both the micropillar feature and the CNT-implanted electrode configuration. Little loss on the cell viability is observed in different treatments (BE: 88.7% ± 0.7%; CNT: 81.4% ± 2%; BME: 82.6 ± 0.8%; CNT-BME: 80.2 ± 1.0%), as shown in Figure 4c. This suggests the improvement of the transfection efficiency is not the compromise of viability loss that is commonly seen in an electroporation optimization process.

Benefited from its high cell viability, even for cells loaded with low-dose GFP plasmids during initial CNT-BME treatment, their expression level on GFP protein could also reach detectable levels after extended cell culture. This leverages the overall transfection efficiency above 95% three-day post electroporation (Figure 4d). Besides the high percentage of the

transfected cells to all treated cells (i.e., transfection efficiency), higher average dosage of GFP is also introduced in individual cells after CNT-BME treatment when compared to that in BE cuvette treatment. This is confirmed with the GFP expression level measurement on the mean fluorescence intensity of the entire cell population counted by flow cytometry. Comparing to the BE treatment, the CNT-BME electroporation shows a 22-fold increase on the quantity of GFP plasmids in K562 cells (Figure 4d). Given the fact that a low DNA probe/cell concentration ratio used in this work (i.e., 2 $\mu g/10^6$ K562 cells), this suggests that an averagely high dosage of plasmids was delivered in individual cells via this CNT-BME electroporation, which help boosts the overall transgene expression in those hard-to-transfect blood cells.

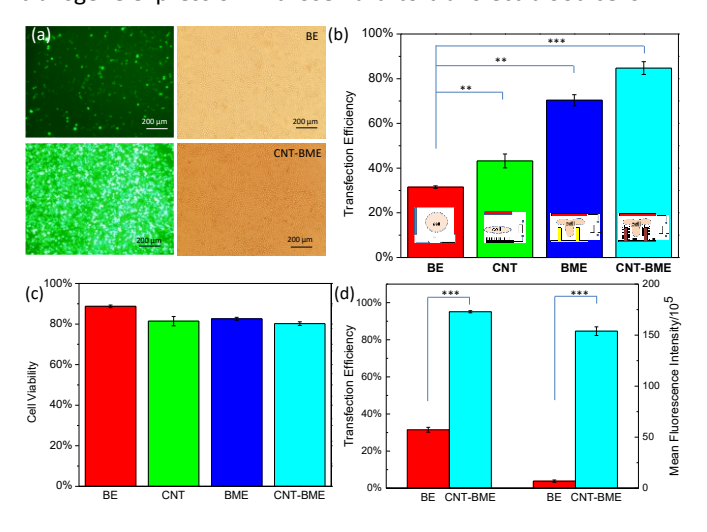


Figure 4. The transfection and cell viability of K562 cells in four different transfection methods with a cell concentration of 107 cells/mL. The phase contrast and fluorescent images (a), quantitative transfection efficiency (b), and cell viability (c) of samples 24 hrs after transfection. (d) The transfection efficiency (i.e., the number percentage of GFP positive K562 cells, left group data in panel d) and mean fluorescence intensity (i.e., average GFP dosage in individual cells, right group data in panel d, which is divided by a factor of 105) 72hour post electroporation. The same color codes are applied in panels b-d for four different electrode setups with their configuration and cell status schematically drawn on each column in panel b (BE: spherical; CNT: squeezed; BME & CNT-BME: squeezed and deformed shapes). Significance t-test was performed with n=3 with **P < 0.01 and ***P < 0.005 and compared to the BE alone treatment.

Enhanced RNA Delivery and Functions

To further demonstrate the effectiveness of CNT-BME to the loading of oligonucleotides in blood cells and their interference roles to target proteins, we further investigated the internalization of siRNA and miRNA probes in both lymphoblast and primary blood cells. K562 cells and blood samples were treated by CNT-BME with 200 pmol miR-29b under the same electroporation conditions. As

shown in Figure 5a, the loading dosage of mature miR-29b in K562 cells by CNT-BME is ~2.5 folds more than that by the commercial system ("BE"). For whole blood cells, such enhancement difference is close to ~3 folds (Figure 5b). As more than 90% of the whole blood cells are red blood cells (RBCs), the result of blood samples reflects mainly the uptake situation of RBCs. These results demonstrate similar delivery enhancement of CNT-BME to RNA probes in different types and sizes of blood cells individually.

To confirm the retention to the interference functions of the loaded oligonucleotides in blood cells, two different examinations were done. One is to investigate the interference of RNA probes to exogenous proteins in cells. This was done by co-transfecting target GFP plasmids and siRNA probes whose sequence could specifically silence GFP expression in K562 cells. The knockdown efficiency of siRNA was evaluated by measuring the expression level of GFP proteins in cells by flow cytometry. As shown in Figure 5c, clear suppression of GFP signal is observed when co-delivering pMaxGFP and 5 pmol corresponding siRNA by both BE and CNT-BME treatments. However, ~38% more GFP expression is turned off by the CNT-BME treatment than that in BE (BE: 25%; CNT-BME: 63% down regulation from their individual control treated with GFP plasmid alone). When the siRNA dosage is increased to 30 pmol, the down regulation level of GFP by the CNT-BME treatment reaches ~90% when compared to 60% from the BE treatment (Figure 5c). It is worth to mention that the down regulation was achieved without sacrifice health of cells (supp Figure 3), and as co-transfection of plasmids and corresponding siRNA was used here, the delivery enhancement on the target reporter gene and its corresponding siRNA occurs simultaneously. In another word, CNT-BME need turn off much more GFP mRNAs like what is shown in Figure 4d than the BE system to reach the similar protein expression level during this down regulation experiment.

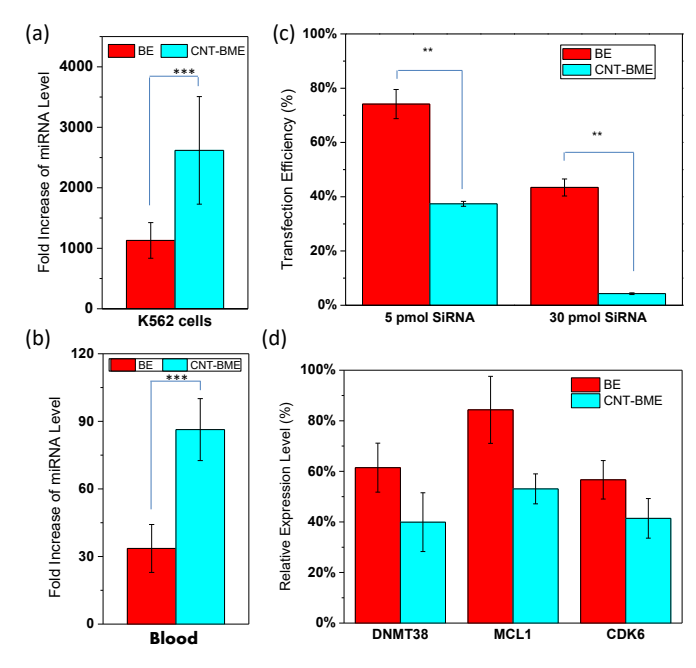


Figure 5. Result for CNT-BME enhanced GFP siRNA and miR-29b delivery in K562 cells and whole blood. (a,b) The loading dosage of miR29b in K562 cells (a) and blood cells (b). The down regulation performance of GFP expression level when

co-transfecting GFP plasmid and the corresponding siRNA probes (c) and the expression levels of DNMT38, Mcl-1, and CDK6 genes after delivering miR29b (d), normalized to their levels in the negative control samples (100%).

We also evaluated the performance of those internalized RNA probes in another way by examining their regulation ability to the levels of endogenous genes which are generally steady in cells. We chose miR29b probes and measured their knock down efficiency on three target genes that are often over expressed in cancer cells: DNMT 3B (DNA methyltransferases members or DNMTs that regulates DNA demethylation pathway), Mcl-1 (Myeloid cell leukemia-1 or Mcl-1, a potent, multidomain anti-apoptotic protein of the B-cell lymphoma family), and CDK-6 (Cyclin-dependent kinase 6, regulating the progression of the cell cycle). As shown in Figure 5d, for cells that were treated by CNT-BME, the level of these target genes was down regulated to ~40% for DNMT3B, ~50% for Mcl-1, and ~40% for CDK6, respectively, all better than what were received in a commercial system (DNMT3B: ~60%; Mcl-1: ~85%; CDK6: ~55%). These results suggest that CNT-BME can introduce more miRNA 29b probes into blood cells so that those targeted endogenous genes in cells can be down regulated to much lower levels by those oligonucleotides.

Cell Size Independence

One unique advance of this CNT-BME treatment lies on its effective transfection on cells of various sizes, which is critical for the success of both classic and whole blood cell therapy. With a size of 6-25 μm in diameter, K562 cells mimick well various types of WBCs used in classic blood cell therapy. Because the FSC signal of flow cytometry reflects cell size (i.e., stronge FSC for large cells), the transfection performance in WBCs of various sizes can be revealed in the dot plots of flow cytometry results versus FSC. As shown in Figures 6a-b and supp Figure 4a, two subgroups events are clearly shown, one represents K562 cells in normal morphologies and the other for irregular shapes (note: dots that have high SSC signal). When compared with the BE treatment (Figure 6a), significantly more FITC-positive events (i.e., light blue dots) are seen after the CNT-BME treatment (Figure 6b), in both event groups of K562 cells and the entire FSC signal range. The enhancement is more significnat for small (low FSC signal) and large (high FSC signal) cells than those medium size ones. This is reasonable as the recommended electroporation protocols of the commercial system must be optimized for effective transfection to the dominated cell size populations. Nonetheless, these results suggest that CNT-BME works effectively to the same type of target cells with large size variation. Their similar overall dot patterns for SSC signals that reflect cell complexity (e.g., cell shape/morphology) suggest that CNT-BME did not impose additional cell shape changes other than electroporation contributes. Further comparison with cell samples electroporated with plain CNT-coated electrodes (the ones have no micropillar array pattern) finds similar signal pattern of the FITC-positive events (supp Figure 4b), confirming the contribution of numerous CNT nanoelectrodes to the overall GFP

positive signals in both cell subgroups with different sizes and morphologies.

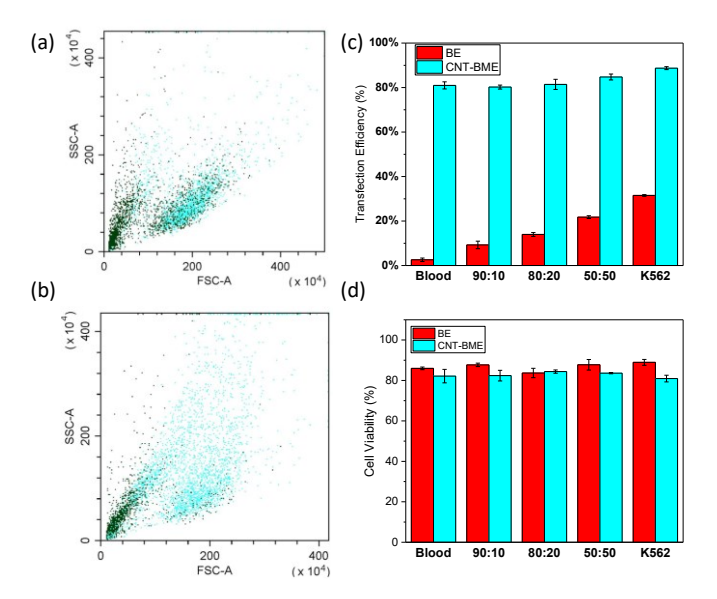


Figure 6. Comparison of transfection impact in individual types and mixtures of blood and K562 cells with CNT-BME and BE treatment. The dot plots of flow cytometry results in BE (a) and CNT-BME treatments (b). GFP transfection efficiency (c) and cell viability (d) in two types of electroporation treatments. In panels (a) and (b), dark green dots are for all events and light blue dots are for GFP positive events.

To further investigate the transfection meddling of other types of cells that have significant size difference to the target cells, mixtures of K562 cells and whole blood cells with at different ratios were used. With their exclusive population dominance in whole blood cells, RBCs of 5-6 µm (90%+) serve as desired meddlesome candidates to target K562 cells on their transfection by CNT-BME. We evaluated GFP plasmid delivery in cell mixtures at three ratios (50/50, 80/20, and 90/10 for whole blood cells/K562 cells). With a total number of 106 cells/sample, the cell mixtures were treated by CNT-BME and BE electroporation with 10 μg pMaxGFP plasmids using the same protocols mentioned early. Because non-nucleated RBCs can not transcribe/translate plasmids, the GFP expression in those mixed cell samples is contributed mainly by GFP plasmids internalized by K562 cells (with minor addition from various WBCs in blood samples). As shown in Figure 6c, the transgene expression level in CNT-BME treated cells retains similar, all 80+% of the defined K562/WBCs cell subgroups, though slightly lower than the case with K562 cells alone. The large presence of RBCs in cell mixtures does not affect much the uptake of plasmids in K562/WBC cells. As comparison, the BE treatment receives 9% (50/50 mixture), 14% (80/20 mixture), and 22% (90/10 mixture) on the pMaxGFP transfection efficiency, respectively, presenting a steady rising on plasmid uptak when more K562 cells are added (Figure 6c). Further confirmation on the health status of the treated cells right after treatment (supp Figure 5) and after extended culturing (Figure 6d) suggests that CNT-BME works well in

complicated blood samples with various cell types, populations, and sizes.

Delivery to Whole Blood Samples

To show the effectiveness of this CNT-BME electroporation in whole blood therapy, the new electrode configuration was also tested with whole blood comprised of various RBCs and WBCs that have significant size differences. As not all cells in whole blood samples have a nucleus to carry out the normal transcription/translation processes (or "transfection" we refer to), the delivery (or loading) efficiency to various blood cells was measured using fluorescence labeled genetic probes. As shown in both fluorescence (Figure 7a) and confocal microscopy (Figure 7b) images, Cy5-labeled GFP mRNA probes were successfully loaded into all three different types of blood cells by CNT-BME. Among blood cells, RBCs are identified from WBCs by their obvious size difference (or FSC signals in flow cytometry, as shown in Figure 7c) while reticulocytes are assorted from erythrocyte among RBCs by their globular shape or FITC signal after TO staining (FITC positive after stained with TO dyes, as shwon in Figures 7b & 7c). Further quantitative analysis by flow cytometry finds that the delivery efficiency is high and consistent (> 85%) in sub-populations of both leukocytes and reticulocytes (Figure 7d). Compared to these blood cells with nuclei, the mRNA encapsulation in erythrocytes is relatively low (~45%), which, though not fully understood, must be tied with the already deformed morphology of those cells and their lack of the double membrane structure (cell and nucleus membrane) that is important for electroporation. Nonetheless, the loading efficiency of GFP mRNA in all three types of blood cells by CNT-BME is much better than that with traditional electroporation setup that uses cuvettes (Figure 7d). Those mRNAloaded blood cells remain highly viable after electroporation, as quantified by live/dead assay (Figure 7e and supp Figure 6). These results prove that the CNT-BME treatment is effective for whole blood samples, important for future whole blood therapy.

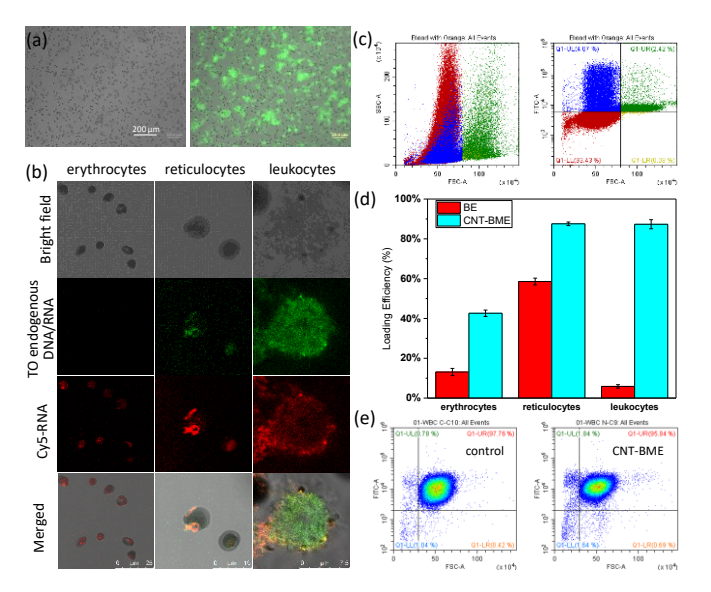


Figure 7. Whole blood delivery of GFP mRNA probes with CNT-BME. (a) Phase contrast and merged fluorescence images of mRNA-loaded whole blood samples. (b) Confocal images of mRNA encapsulated in erythrocytes, leukocytes, and

reticulocytes. Cy5-labeled GFP mRNA (red); thiazole stain (green) of cellular DNA/RNA of reticulocytes and leukocytes. (c) flow cytometry dot-plots to present subgroups of erythrocytes (red), leukocytes (green), and reticulocytes (blue), distinguished by FSC and FITC signals (note: both reticulocytes and leukocytes were stained with TO for FITC positive events). (d) loading efficiency of Cy5-labeled GFP mRNA in different blood cell types; (e) live/dead instant cell viability based on calcein signal (FITC positive) in blood cells, with various colors indicating cell number density.

In case a large number of cells are required (e.g., treated cells are injected back to patient in clinical practice of whole blood therapy), the CNT-BME setup can be conveniently scaled up by assembling micropatterned electrodes in arrays and operated in a microfluidic format³⁹. This can be done by integrating the CNT-coated micropillar array electrodes as part of the top and bottom walls of a slit-type microfluidic channel (supp Figure 7). When cells flow through the electroporation zone, they receive desired pulse treatment. With a small array of 40 microchannels, a targeting throughput of ~10¹⁰ cells/min could easily reach, assuming a reasonable blood flow of 5 ml/min and a diluted blood solution of 5×10⁷ cells/ml (1/100 dilution of blood, close to what was used in this work) are applied (the total cell number/min = 40×5 ml/min $\times 5 \times 10^7$ cells/ml = 10^{10} cells/min). This yields ~ 120 mL/hr blood treatment (assuming ~5×109 cells/ml in normal blood), which is enough for whole blood therapy applications.

Robustness of CNT-implanted Electrodes by EIS Analysis

To guarantee continuous operation and transfection reproduction, robust conductive coating is essential. The stability of CNTs implantation on the micropillar array surface was examined by EIS tests on fresh and used CNTs-BME electrodes as well as plain electrodes coated with CNTs but no micropillar pattern (denoted as "CNT"). As shown in Figure 8a, the Nyquist plots of all three cases exhibit a similar shape, i.e., a semicircle followed by a straight line. But the electrode without micropillars (brown dots) has a charge transfer resistance (i.e., the diameter of the semicircle on the real axis) over four times larger than the ones with micropillar array (pink and blue dots), suggesting that micropattern significantly reduces the electrode resistance. But for both micropatterned electrodes, the used one (pink dots) has a similar charge transfer resistance with the fresh electrode (blue dots), considering the measuring errors. Their identical slope in the linear region of the Nyquist plots also indicates the similar mass transfer (i.e., diffusion) situation when reusing those 3D CNT-implanted electrodes. These results confirm the partial implanted CNT coating layer is very stable to help retain the excellent conductivity of the fabricated electrode even after high-voltage pulse strikes, which is attributed to the infiltration of polymer resin in the entangled CNT network that bolsters the exposed CNTs by the cross-linked SU-8 resin base of the composite electrode (Figure 2e_iii). The implanted CNT nanoelectrodes are very robust even after periodical tests with high

current spikes (inset of Figure 8a and supp Figure 8) and thus, generate reproducible performance in electroporation tests.

An equivalent circuit model was used to fit the Nyquist plot data for each case to extract the solution resistance (Rs), charge transfer resistance (Rp), Warburg impedance (W), and capacitance of the electrode/electrolyte interface (CPEs). As shown in Figures 8b, the value of Rs and charge transfer resistance (Rp1 + Rp2) for new and used micropatterned electrodes is similar (new: 4.31 \pm 0.18 k Ω ; used: 4.88 \pm 0.33 kΩ), way smaller than the plain, CNTs-coated electrodes ("CNT": 20.65 \pm 2.06 k Ω). The Warburg impedance (W) for the electrodes with micropillar pattern, on the other hand, is much larger than that of the electrode without micropillars. All these results confirm that the micropillar array pattern indeed significantly promotes the electrical conductivity for the composite electrodes. The data fitting also suggests two distinct regions exist within the composite electrode, namely Region 1 and Region 2 with their corresponding Rp and CPE values: some areas have micropillar patterns while others have only CNTs paved on the substrate surface. The smaller "N" value for the two CPEs in the equivalent circuit model of the micropatterned electrode also endorses the surface heterogeneity of the composite electrodes with patterned and non-patterned regions and its deviation from a pure capacitor.

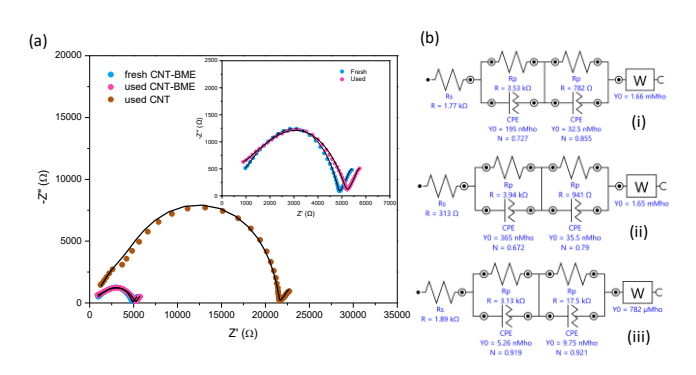


Figure 8. Nyquist plots of CNT-implanted electrodes with and without micropillar array pattern (a) and the corresponding equivalent circuit model fitting (b). Fresh electrode with micropillar pattern: blue dots in panel a and I in panel b; used electrode with micropillar pattern: pink dots in panel a and II in panel b; used electrode without micropillar pattern: brown dots in panel a and III in panel b.

Conclusions

In summary, CNTs are implanted in polymer micropillars to form a 3D nanotube-in-micropillar electrode configuration and was used for electroporation toward blood cell therapy. In one step, an array of polymer micropillars was fabricated by a micromolding process with CNTs successfully implanted on the pattern surface through resin infiltration. Such a partial embedment configuration provides robust CNT coating, leaving exposed CNTs on both the top and side surface of micropillars as nanoelectrodes while the rest inside polymer as the conductive base. When used in cell electroporation, the micropillars get cells sagged in with their bilayer membrane

structure stretched to maximize the poration area. The CNT nanoelectrodes vertically protrude against the cell membrane surface everywhere for easy breakdown. With a regular microarray pattern on the electrode, this 3D electroporation system allows the permeable area on the cell membrane to vary with the size of cells but independent of their random settling status. Such universal disruption is further advanced by the CNT nanoelectrodes to nanometer resolution. With all these advantages, this CNT-BME system overcomes the cell membrane capacitance more effectively so that both the delivery of plasmids and RNA probes get improved significantly on blood cells of different types as well as their mixtures. Compared to the traditional electroporation treatment, much higher dosage of genetic probes was introduced in blood cells, which regulates better the expression levels and functions of both exogenous and endogenous proteins. This 3D nanoelectrodes could advance not only efficient and convenient non-viral delivery route for blood cell therapy, but also provide an effective and safe manufacturing approach of other cell-related medicine.

The fabrication method reported here also provides a new way for robust anchoring of nanofeatures on polymer micropattern surface. Besides the excellent electrical conductivity it offers to electronic devices, the partial implantation status of CNTs makes stable conductive coating on electrodes, unlike thin film introduced by many traditional processes that is often seen gradually detached from substrates when experiencing high voltage/current spikes and/or repeated/continuous testing. Although it was demonstrated on rigid substrates (e.g., Si) in this work, there is no technical barrier to apply this microfabrication method on soft substrates as flexible electronics that require or prefer conformal attachment on nonplanar surfaces and/or tolerance of quick and frequent deformation or geometry changes of substrates. It may broadly benefit many bioelectronics and human-machine communication applications such as smart electronic skins and artificial intelligence to dynamically track human motions and health, key technology toward in-situ healthcare, robotics, and augmented/virtual reality. 40,41

Conflicts of interest

"There are no conflicts to declare".

Supplementary information

Supplementary figures on COMSOL simulation geometry, SEM images of CNT-coated plain electrode, flow cytometry results and microscopic images on transfection and cell viability after treatment, microfluidic arrays design for continuous operation, and EIS tests of multiple new and used devices.

Acknowledgements

This work was supported by National Science Foundation [1662735, OIA-1541079]

Notes and references

- 1 P.T. Rowley, J.A. Morris, J. Bio. Chem. 1967, 242, 1533.
- 2 S. Corinti, L. Chiarantini, S. Dominici, M.E. Laguardia, M. Magnani, G. Girolomoni, *J. Leuko. Bio.* 2002, **71**, 652-658.
- 3 A. Banz, M. Cremel, A. Mouvant, N. Guerin, F. Horand, Y. Godfrin, *J. Immunother.* 2012, **35**, 409-417.
- 4 M. Moenner, M. Vosoghi, S. Ryazantsev, D. G. Glitz, *Blood Cells Mo. Dis.* 1998,**24**, 149-164.
- 5 K. Phua, H. Staats, K., Leong, S. K. Nair, *Sci. Rep.* 2015, **4**, 5128
- 6 K.K. Phua, D. Boczkowski, J. Dannull, S. Pruitt, K.W. Leong, S.K. Nair, Adv. Health. Mater. 2014, 3, 837-842.
- S. Ravilla, B. R. Chandu, S. Nama, B. Nagaveni, J. App. Pharm. Sci. 2012, 2, 166-176.
- 8 N. Rains, R.J. Cannan, W. Chen, R.S. Stubbs, Hepatogastroenterology 2000, 48, 347-351.
- 9 I.M. Verma, N. Somia, Nature 1997, 389, 239-242.
- 10 E. Marshall, Science 1999, 286,2244-2245
- 11 J. Gehl, Acta Physiol. Scand. 2003, 177, 437-447.
- 12 T. Kotnik, F. Bobanovic, D. Miklavcic, *Bioelectrochem. Bioenerg*. 1997, **43**, 285-291.
- 13 P. Wheater, Blood, in Functional Histology, Churchill Livingstone, Barcelona, 1980, 24–37.
- 14 Y. Huang, B. Rubinsky, Sens. Actuators A 2001, 89, 242-249.
- 15 S.C. Yang, K.S. Huang, H.Y. Chen, Y.C. Lin, *Sens Actuators B* 2008, **132**, 551-557.
- 16 M. Khine, A. Lau, C. Ionescu-Zanetti, J. Seo, L. P. Lee, *Lab Chip* 2005, 5, 38-43.
- 17 H. Lu, M. A. Schmidt, K. F. Jensen, Lab Chip 2005, 5, 23–29.
- 18 Y. Zhan, J. Wang, N. Bao, C, Lu, Anal. Chem. 2009, 81, 2027-2031.
- 19 Z. Fei, S. Wang, Y. Xie, B. Henslee, C. Koh, L.J. Lee, *Anal. Chem.* 2007, **79**, 5719-5722.
- 20 E.G. Guignet, T. Meyer, Nat. Methods 2008, **5**, 393 395.
- 21 D. Zhao, D. Huang, Y. Li, M. Wu, W. Zhong, Q. Cheng, X. Wang, Y. Wu, X. Zhou, Z. Wei, Z. Li, Z. Liang, *Sci. Rep.* 2006, 6 18469.
- 22 C. Dalmay, J. Villemejane, V. Joubert, O. Français, L.M. Mir, B.L. Pioufle, Sens. Actuators B 2011, 160, 1573-1580.
- 23 M. Wu, D. Zhao, W. Zhang, H. Yan, X. Wang, Z. Liang, Z. Li, Sci. Rep. 2013, 3, 3370/1-7.
- 24 L. Chang, D. Gallego-Perez, C. Chiang, P. Bertani, T. Kuang, Y. Sheng, et al, *Small* 2016, **12**, 5971-5980.
- 25 Y. Zu, S. Huang, Y. Lu, X. Liu, S. Wang, Sci. Rep. 2016, 6, 38661.
- 26 Z. Chen, M.A. Akenhead, X. Sun, H. Sapper, H.Y. Shin, B.J. Hinds, *Adv. Health. Mater.* 2016, **5**, 2105-2112.
- 27 P. Garcia, Z, Ge, J. L. Moran, C. R. Buie, *Sci. Rep.* 2016, **6**, 21238/1.11
- 21238/1-11. 28 N. Bhattacharjee, L.F. Horowitz, A. Folch, *Appl. Phys. Lett.*
- 2016, **109**, 163702/1-5. 29 J.A. Kim, K. Cho, Y.S. Shin, N. Jung, C. Chung, J.K. Chang,
- Biosens Bioelectron 2017, **22**,3273-3277.

 30 S.K. Kim, J.H. Kim, K.P. Kim, T.D. Chung, *Anal. Chem.* 2007,
- **79**, 7761-7766. 31 S. Huang, H. Deshmukh, K.K. Rajagopalan, S. Wang,
- Electrophoresis 2014, **35**, 1837-1845.
- 32 D. Gallego-Perez, S. Ghatak, V. Malkoc, N. Higuita-Castro, S. Gnyawali, L. Chang, et al, *Nat. Nanotech.* 2017, **12**,974-979.
- 33 Q. Zheng, D. C, Chang, Biochim Biophys Acta (gene structure and expression) 1991, **1088**, 104-110.
- 34 Z. Fei, X. Hu, H.W. Choi, S. Wang, D. Farson, L. J. Lee, *Anal. Chem.* 2010, **82**, 353-358.
- 35 K. Kulangara, Y. Yang, J. Yang, K.W. Leong, *Biomaterials*. 2012, **33**, 4998-5003.
- 36 S. Wang, X. Zhang, W. Wang, L. J. Lee, Anal. Chem. 2009, 81, 4414-4421.

- 37 J.A. Kim, K. Cho, M.S. Shin, W.G. Lee, N. Jung, C. Chung, J.K. Chang, *Biosens. Bioelectron.* 2008, **23**, 1353–1360.
- 38 J. Chen, Y. Zu, K. Rajagopalan, S. Wang, *Nanotechnology* 2015, **26**, 235603/1-8.
- 39 Y. Zu, X. Liu, A. Chang, S. Wang, *Bioelectrochem*. 2020,132, 107417.
- 40 H. Li, S. Gu, Q. Zhang, E. Song, T. Kuang, F. Chen, X. Yu, L. Chang, *Nanoscale* 2021, **13**, 3436-3453.
- 41 A. Chang, X. Liu, Y. Pei, C. Gong, P. Arumugam, S. Wang, Electrochimica Acta 2021,368, 137632.